https://doi.org/10.5194/egusphere-2026-3900
Preprint. Discussion started: 29 July 2026


# Evolution of basal terraces in the cold-cavity of Ekström Ice Shelf in East Antarctica

Rebecca Schlegel[1], Johannes Noll[1], Leah Sophie Muhle[1], Christian T. Wild[1,2], Falk M. Oraschewski[1,3], Olaf Eisen[4,5], and Reinhard Drews[1]

[1]Department of Geosciences, University of Tübingen, Tübingen, Germany
[2]Department of Atmospheric and Cryospheric Sciences, University of Innsbruck, Austria
[3]Geological Survey of Denmark, Copenhagen, Denmark
[4]Alfred Wegener Institute, Helmholtz Centre for Polar and Marine Research, Bremerhaven, Germany
[5]Department of Geosciences, University of Bremen, Bremen, Germany

**Correspondence:** Rebecca Schlegel (Rebecca.Schlegel@uni-tuebingen.de)

**Abstract.** Basal melting beneath Antarctic ice shelves drives ice-shelf thinning, impacts buttressing of inland ice streams, and contributes to grounding line retreat, thus affecting the rate of global sea-level rise. Yet, processes controlling the spatial variability of basal melt remain poorly constrained because observations of the evolving basal topography are sparse. One important but poorly understood feature are basal terraces. Here, we present a ground-penetrating radar (GPR) dataset imaging the evolution of basal terraces in the cold-water cavity beneath Ekström Ice Shelf. The quasi three-dimensional GPR data are complemented by an autonomous phase-sensitive radio echo sounder (ApRES) record and airborne radar data. No significant changes in the basal topography are observed between the two field seasons. Basal melt rates at the terrace roofs are less than a meter per year and lower than the regional average, ApRES-derived monthly variability ranges between 0.3 and 0.6 m a$^{-1}$. A weak off-angle reflector suggests that melt rates at the terrace walls may be higher, but not higher than 4 m a$^{-1}$. Overall, basal terracing occurs predominantly near the grounding zone, and the ice–ocean interface becomes smooth further offshore. We conclude that basal terraces occur beneath both warm- and cold-cavity ice shelves and that the low melt rates at terrace roofs are consistent with previous studies suggesting that a stratified ocean layer shields the ice base from oceanic heat transport. However, melt rates at the terrace walls are also low. Therefore, our results suggest that once basal terraces are created near the grounding zone, they may enter a stagnant mode and subsequently advect with the ice-shelf flow towards the ice edge where they eventually disappear.

## 1 Introduction

Ice shelves, the floating extensions of grounded ice streams, buttress the flow of inland ice toward the ocean. Thinning (Gudmundsson et al., 2019; Reese et al., 2018) or retreat (Mitcham et al., 2022; Greene et al., 2022b; Joughin et al., 2021) of ice shelves can reduce this buttressing effect, accelerating ice discharge and thus increasing rates of sea-level rise (Scambos et al., 2004). In Antarctica, ocean-driven melting at the ice shelf base (hereafter referred to as basal melting) alongside iceberg calving from the ice edge are the major drivers of ice shelf mass loss (Davison et al., 2023; Greene et al., 2022a). However, the

https://doi.org/10.5194/egusphere-2026-3900
Preprint. Discussion started: 29 July 2026


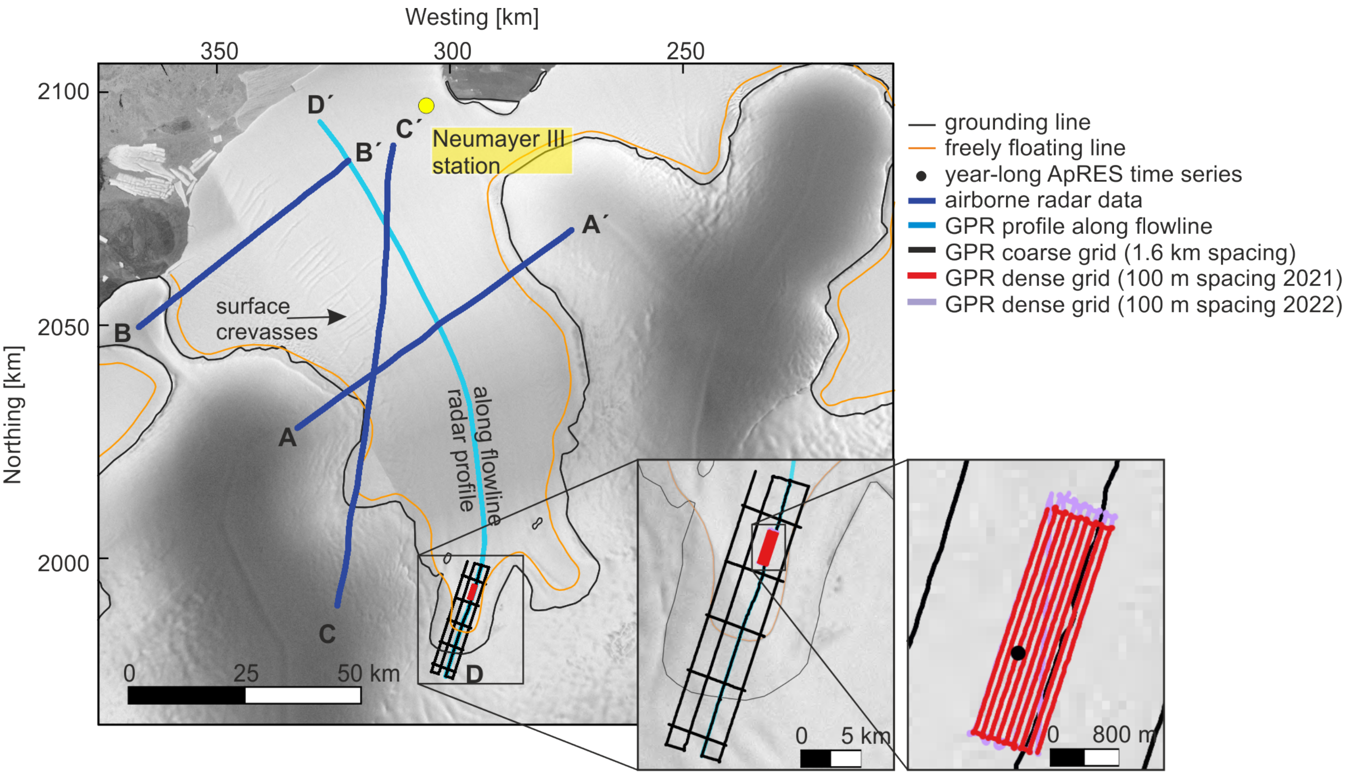


**Figure 1.** Ekström Ice Shelf with different radar surveys. Along-flow GPR profile (cyan), and across-flow airborne radar tracks (dark blue, ultra-wide band and accumulation radar). The inset shows a zoom-in on the coarse GPR grid and the dense GPR grid, which were repeated in consecutive seasons (Fig. B1). Background is from the RADARSAT-1 Antarctic Mapping Project (RAMP) (Jezek et al., 2003).

spatial and temporal variability of basal melt remains one of the largest uncertainties in predicting ice sheet evolution (Hanna et al., 2024; IPCC, 2022).

Basal melt rates are controlled by the temperature and salinity gradients between the ocean water and the ice–shelf base, and the amount of turbulence in the water that can break an otherwise strongly stratified boundary layer resulting from pooling of buoyant meltwater beneath the ice base (Pritchard et al., 2012; Stewart et al., 2019; Malyarenko et al., 2020; Rosevear et al., 2022). Ocean circulation patterns accessing differently shaped sub-ice-shelf cavities create strong regional contrasts: ice shelves in West Antarctica generally experience higher melt rates due to intrusions of relatively warm water, whereas ice shelves in East Antarctica are typically bathed in colder waters. On regional and sub-regional scales, basal melt rates vary by nearly an order of magnitude both within and between ice shelves (Watkins et al., 2021; Adusumilli et al., 2020). Expressions of this local variability at sub-kilometer scales include distinct basal features such as ice–shelf channels (Drews, 2015; Alley et al., 2016; Drews et al., 2017; Zhou et al., 2025) and basal terraces (Dutrieux et al., 2014, 2013; Grima et al., 2019; Schmidt et al., 2023; Wåhlin et al., 2024; Rignot et al., 2025b). Ice–shelf channels are curvilinear zones of thinned ice, typically a few kilometers wide, that align with the along-flow direction and sometimes extend across the entire ice shelf (Drews, 2015). In contrast, basal

https://doi.org/10.5194/egusphere-2026-3900
Preprint. Discussion started: 29 July 2026


terraces have no known orientation relative to ice flow, are characterized by abrupt changes in ice thickness across terrace walls, and are interconnected by near-horizontal, smooth terrace roofs. Bridging stresses maintain a local imbalance from hydrostatic equilibrium across spatial scales of one local ice thickness. Consequently, basal terraces are not necessarily detectable from the ice–shelf surface alone.

Since their initial discovery (Dutrieux et al., 2014), substantial progress has been made in understanding the formation mechanisms of these distinctive basal features. Variations in basal ice-shelf slope are an important control on vertical mixing and oceanic heat transport to the ice base (Anselin et al., 2024). For basal terraces specifically, Schmidt et al. (2023) present observations from an underwater vehicle near the grounding zone of Thwaites Glacier. These suggest that basal terraces evolve from small thickness perturbations at the grounding line, with strongest melting occurring at terrace walls, while ocean stratification suppresses melting at terrace roofs. Grima et al. (2019) formulate a similar hypothesis based on the disturbed topography that they observe near basal terraces below the Ross Ice Shelf. In their case, local thickening of the ice shelf may additionally act as a seed point for terrace formation. Using an underwater vehicle, Wåhlin et al. (2024) observed oceanographic conditions beneath the Dotson Ice Shelf and proposed that at least parts of the terraces are linked to episodic intrusions of warm surface waters. An interplay of crevasse formation near the grounding zone and differential basal melting and/or refreezing is hypothesized as a formation mechanism by Gillespie et al. (2017) based on GPR data downstream of Darwin Glacier. Basal terracing has also been observed beneath Greenlandic ice shelves (Rignot et al., 2025a), demonstrating their widespread appearance.

One limitation in our current understanding of basal terraces is the lack of repeat observations quantifying the temporal evolution of a specific terrace field. Although hypothesized, it has not been directly observed that melt rates on terrace roofs are smaller than melt rates on terrace walls, nor how these features evolve over time. To address this, we imaged a basal terrace field at the Ekström Ice Shelf (East Antarctica) during two consecutive seasons using a dense grid of GPR profiles to resolve the three-dimensional topography and temporal changes. In addition, we deployed a continuously operating autonomous phase-sensitive radio echo sounder (ApRES, Brennan et al., 2014) above a terrace roof to monitor basal melting on weekly to annual timescales. We further contextualize our findings with airborne radar transects that image basal terraces in other regions of the ice shelf and provide insights about how basal terraces evolve during ice advection.

## 2 Study Area

The Ekström Ice Shelf is one of several ice shelves that traverse the coast of Dronning Maud Land in East Antarctica. Today's surface velocities range from $100\,\mathrm{m\,a^{-1}}$ to $230\,\mathrm{m\,a^{-1}}$ so that the advection time from the grounding line to the ice shelf front is typically less than 800 a. There is no evidence for strong dynamic changes since the last glacial maximum (Drews et al., 2013) and the entire catchment is comparatively robust to ice-dynamic perturbations (Schannwell et al., 2019).

The oceanographic context along the Dronning Maud Land coast is determined by a narrow continental shelf with Warm Deep Water masses flowing along the steep continental slope. At Ekström Ice Shelf, inland-sloping bathymetric canyons extend from the inner continental shelf to the present-day grounding line (Smith et al., 2020). These allow strong interactions between the sub-shelf cavity and the coastal current, potentially making this ice shelf susceptible to warming ocean waters (Gille, 2008)

https://doi.org/10.5194/egusphere-2026-3900
Preprint. Discussion started: 29 July 2026


and to increased upwelling of Circumpolar Deep Water (Holland et al., 2008). Today, in-situ measurements within the cavity show cold water temperatures -1.9 °C (Smith et al., 2020). The resulting lack of heat input from warm waters is consistent with a low shelf-averaged basal melt rate. The highest local melt rates are found close to the grounding line and near the German research station Neumayer III with values exceeding $3\,\mathrm{m\,a^{-1}}$, while they decrease to below $0.5\,\mathrm{m\,a^{-1}}$ in the interior of the ice shelf (Neckel et al., 2012; Moss et al., 2025; Adusumilli et al., 2020). Basal melting is higher in winter and spring, likely linked to sea-ice formation and a strengthening of an ice shelf water plume; the far-field forcing by ambient ocean temperatures is secondary (Zeising et al., 2025). Evidence from internal stratigraphy preserved within the ice column suggests that basal melt rates were stable on centennial timescales (Moss et al., 2025). Due to the comparatively low melt rates, Ekström Ice Shelf still has ice sheet meteoric ice at its base up until more than 100 km away from the grounding line. Further seawards, the ice shelf is sustained by local meteoric ice only (Višnjević et al., 2025; Moss et al., 2025).

## 3 Data & Methods

To monitor temporal changes of the basal terrace geometry, we collected GPR grids near the grounding line in two consecutive field seasons (section 3.1). This enables us to determine the yearly average basal melt rates using mass conservation in a Lagrangian reference frame (section 3.5). We also positioned an ApRES system in the center of the GPR grid to detect the temporal variability of basal melting at a fixed location that is advecting with the ice flow (section 3.4). We use spatially more extensive GPR and airborne radar profiles to estimate where basal terraces occur along and across the ice shelf (section 3.3) and their imprint on the basal roughness (section 3.2).

### 3.1 Imaging of the basal terrace geometry using GPR radar

In the field seasons 2021/22 and 2022/23, we collected GPR data using an impulse radar system (PulseEKKO, 50 MHz centre frequency) towed behind a snowmobile at a speed of approximately $10\,\mathrm{km\,h^{-1}}$. We distinguish three profile types (Figure 1): (1) A dense GPR grid in the grounding zone covering $\sim$3 km$\times$800 m with nine along-flow profiles spaced 100 m apart and surveyed in both seasons (red and purple line), (2) a coarse GPR grid with 1.5 km spacing of along- and across-flow profiles, acquired only in the first season (black lines), and (3) a longer along-flow profile extending $\sim$100 km from the grounding zone to the calving front, initiated over 60 km in 2021/22 and completed downstream in 2022/23 (cyan line, Moss et al., 2025).

We processed radar data of the three profile types in a similar manner, which included averaging of several traces to a common 2.5 m posting for the grids and 5 m posting for the along-flow profile to account for variations in driving speed. We followed standard radar-processing workflows in ReflexW (Sandmeier Geophysical Software, 2024), including removal of the pre-trigger, bandpass filtering (with a passband between 30–60 MHz), correction for geometric spreading, automatic gain control, and finite-difference time-domain migration to correct for off-nadir reflections (center frequency of 50 MHz and migration velocity of $0.168\,\mathrm{m\,ns^{-1}}$). We geolocated radar traces with a single-frequency GPS system with the antenna mounted on the snowmobile. For the dense grid, we installed additional bamboo flags at the profile turning points in the first season and used as guidance for the second season to improve navigation. We manually picked the rugged ice–ocean interface with a

https://doi.org/10.5194/egusphere-2026-3900
Preprint. Discussion started: 29 July 2026


particular focus on clearly defining the corner points of the terrace roofs. In both dense grid datasets, we additionally picked three distinct internal reflection horizons spanning the near-surface stratigraphy at average depths of about 15 m, 30 m, and 75 m, respectively. We use these as a proxy for spatial variability in surface accumulation rate and to account for ice advection.

### 3.2 Basal roughness along GPR flowline

To quantify basal geometry changes along the GPR flowline radar profile (cyan line Fig. 1), we calculate the basal spectral roughness $R$ as (Watkins et al., 2021)

$$R = \sqrt{\int_{k_1}^{k_2} S(k)dk}\,. \tag{1}$$

Here, $k$ is the wavenumber and $S(k)$ the power spectral density. We determined the itegration limits $k_1 = 0.0003\,\mathrm{m}^{-1}$ and $k_2 = 0.1\,\mathrm{m}^{-1}$ by trace spacing and profile length. To spatially resolve $R$ along the flowline, we calculated $S(k)$ for overlapping 3000 m segments along the radar profile. We obtained the power spectral density for each segment by first linearly detrending the data and then applying the Fast Fourier Transform.

### 3.3 Airborne radar data for ice-shelf wide context

To better contextualize the observations of the localized GPR coarse and dense grids, we used data from the Alfred Wegener Institute's airborne ultra-wide band and accumulation radar (Franke et al., 2022, 2026). Both radars detect the ice–ocean interface throughout the profiles. The accumulation radar data were recorded in 2014 with a vertical resolution of approximately 1 m and a horizontal spacing of approximately 13 m (Franke et al., 2026). The ultra-wide band radar data were collected in 2023 in sounding mode and with an approximate horizontal trace spacing of 15 m. Both of these comparatively new radar systems have significantly better imaging capacities than the older radar systems in which terracing cannot be easily identified. These data and details of the underlying technical aspects are available through the Marine Data Portal (Franke et al., 2026).

### 3.4 Weekly average of basal melt rates at a terrace roof using ApRES

We derived weekly averaged melt rates from a continuous ApRES time series by decomposing the observed thickness change into dynamic strain thinning and basal melting (Vaňková et al., 2023; Lindbäck et al., 2025; Zeising et al., 2025). We acquired ApRES data in the centre of the dense grid (S 71° 36.9565' W 8° 25.9803') at a location ultimately identified as a terrace roof (Fig. 4a). The system transmitted a linear frequency-modulated chirp from 200 to 400 MHz over 1 s. We acquired ApRES data in polarimetric mode (Ershadi et al., 2022). However, we do not consider the polarimetric aspect further since basal melt rates are derived from a single antenna orientation (HH). We recorded bursts of 40 chirps every 3 h from 9 January 2022 to 2 February 2023. We averaged chirps within each burst to improve the signal to noise ratio. Processing followed the methods of Brennan et al. (2014) and Stewart et al. (2019), using a Blackman window and a pad factor of 8. We assumed a constant radio-wave velocity of $0.168\,\mathrm{m\,ns}^{-1}$ to convert traveltime to depth.

https://doi.org/10.5194/egusphere-2026-3900
Preprint. Discussion started: 29 July 2026


To determine vertical strain rates, we cross-correlated discrete 6 m depth bins with 3 m overlap between consecutive bins across ApRES repeat measurements to track the vertical displacement of internal reflectors throughout the ice column. Assuming nadir reflections and therefore purely vertical displacements, we obtained vertical displacement rates for each depth bin by fitting a linear function to the displacement time series and retained only bins with a mean cross-correlation coefficient greater than 0.95. We excluded the upper 80 m to avoid the influence of firn densification and fitted a linear function to the resulting profile of vertical velocities to estimate the displacement rate of the ice base purely due to strain deformation (Fig. 6c). The slope of this linear fit corresponds to the vertical strain rate, $\dot{\varepsilon}_z$, which is also used in section 3.5. The residual between the measured ice-base displacement rate and the displacement rate predicted from strain deformation alone provides the basal melt rate $\dot{b}$, assuming that the basal reflection occurs at nadir.

### 3.5 Yearly average of basal melt rates across a basal terrace field from Lagrangian mass conservation

As we expect basal melting at terraces to introduce abrupt regional ice thickness changes over time, we here derived melt rates from two time slices in ice thickness, rather than using mass conservation in an Eulerian framework (Moholdt et al., 2014; Berger et al., 2017). The ice thickness profiles $H_i$ obtained from the high-resolution GPR grids (Figure 4a,b) allow us to derive basal melt rates $\dot{b}$ using mass conservation in a Lagrangian reference frame

$$\dot{b} = \frac{DH_i}{Dt} + H_i(\nabla \cdot \mathbf{u}) - \dot{a}\,. \tag{2}$$

Here, $\frac{DH_i}{Dt} = \mathbf{u} \cdot \nabla H_i$ represents the Lagrangian thickness change based on the horizontal velocity field $\mathbf{u}$ and $\dot{a}$ denotes the surface accumulation rate (in ice equivalent units). All variables have an implicit spatial dependence, i.e., $\dot{a} = \dot{a}(\boldsymbol{x})$. We calculated Lagrangian thickness change by differencing $H_i$ from 2022/23 and 2021/22 after applying a backward shift to account for horizontal advection (Figure 4c). Direct measurements of horizontal advection could have been obtained from the displacement of stakes installed on the surface of the Ekström Ice Shelf; however, such data were not acquired during this period. Therefore, we determined the backward shift by aligning the shapes of internal reflection horizons in the two surveys, assuming that these horizons remained stable over the one-year interval. We identified internal reflection horizons at three different depths in both datasets, and shifted the 2022/23 horizons backward to achieve the best alignment with the corresponding 2021/22 horizons while minimizing residual differences. This approach avoids using the ice–ocean interface for alignment, as it may undergo substantial temporal changes in regions where basal terraces experience strong basal melting. The resulting alignment yields a horizontal offset of 154 m. An independent estimate of horizontal advection can be obtained from the displacement of the ApRES over the same one-year period, which was 146 m a$^{-1}$. After shifting the 2022/23 profiles, the radar postings from the second season were interpolated onto the postings of the first season, resulting in two ice-thickness profiles with consistent geometries. For incompressible ice, the flux divergence can be expressed in terms of horizontal ($\dot{\varepsilon}_x$, $\dot{\varepsilon}_y$) or vertical ($\dot{\varepsilon}_z$) strain rates:

$$\nabla \cdot \mathbf{u} = \frac{\partial u_x}{\partial x} + \frac{\partial u_y}{\partial y} = \dot{\varepsilon}_x + \dot{\varepsilon}_y = -\dot{\varepsilon}_z\,. \tag{3}$$

https://doi.org/10.5194/egusphere-2026-3900
Preprint. Discussion started: 29 July 2026


The dense grid extends about three kilometers along flow, which did not allow for calculation of the velocity gradient based on satellite-derived velocities (differencing closely spaced pixels amplifies noise (Berger et al., 2017)). Instead, we assumed a spatially uniform strain rate across the grid and approximated it using the more robust vertical strain rate $\dot{\varepsilon}_z$ derived from ApRES measurements (section 3.4).

Direct measurements of $\dot{a}$ were unavailable. Therefore, we adopted a reference value of $0.5\,\mathrm{m\,a^{-1}}$, consistent with nearby stake-line observations (Fuchs, 2026; Mengert, 2018) and internal radar stratigraphy (Moss et al., 2025). Applying the shallow-layer approximation (Waddington et al., 2007), we scaled this value according to the depth of the internal radar reflection horizons to maped the spatial variability across the dense grid.

## 4 Results

### 4.1 Topography of basal terraces beneath Ekström Ice Shelf

We first combine the along-flow GPR profile with the across-flow airborne data to identify the ice-shelf wide distribution of basal terraces beneath Ekström Ice Shelf. The primary challenge is to distinguish the basal terraces from the basal crevasses. Basal terraces are identified by their near-horizontal roofs, which appear as bright radar reflectors spanning from tens to hundreds of meters. Adjacent terrace roofs are separated by abrupt thickness variations, and the connecting terrace walls are typically several tens of meters high. In contrast, basal crevasses are generally more gently sloped and, in some cases, incise more deeply upward into the ice shelf. Crevasses may also include terraces along their side walls (Gillespie et al., 2017).

In the airborne accumulation radar data, basal terraces are clearly visible in an across-flow profile within the mid-shelf region (Fig. 2a). Further offshore, terraces are no longer evident. Instead, the ice—ocean interface appears mostly smooth and is only occasionally intersected by basal crevasses (Fig. 2b). Many of these crevasse features correspond to a strain-induced crevasse field that is also visible at the surface on the western side of the Ekström Ice Shelf (Fig. 1). The ultra-wideband radar data show that basal terraces are prevalent near the grounding zone and extend into the mid-shelf region, whereas farther offshore the ice—ocean interface becomes uniformly smooth (Fig. 2c).

Although terrace roofs are visible in the airborne radar profiles, their small-scale geometry cannot be resolved because the along-track spacing is coarse in comparison to the GPR. In the along-flow GPR profile, individual terrace roofs can be traced continuously from about 5 km downflow of the the grounding line (Fig. 2d) to approximately 90 km downstream in the along-flow direction. The roofs are clearly offset in depth relative to one another, and the magnitude of these offsets decreases downstream, consistent with observations from the airborne datasets. More quantitatively, along the along-flow transect (Fig. 3a), roughness is highest near the grounding line ($\sim 10^{-2}$) and decreases approximately exponentially with distance downstream (appearing near-linear in log-space; Fig. 3b). Terrace walls reach several tens of meters in height, and terrace roofs are nearly horizontal near the grounding zone (Fig. 3c). In the mid-shelf region, however, terrace roofs appear tilted and wider, and terrace walls rarely exceed 10 m in height (Fig. 3d), and at approximately 40 km from the ice–shelf front, they are no longer observable (Fig. 3e).

https://doi.org/10.5194/egusphere-2026-3900
Preprint. Discussion started: 29 July 2026


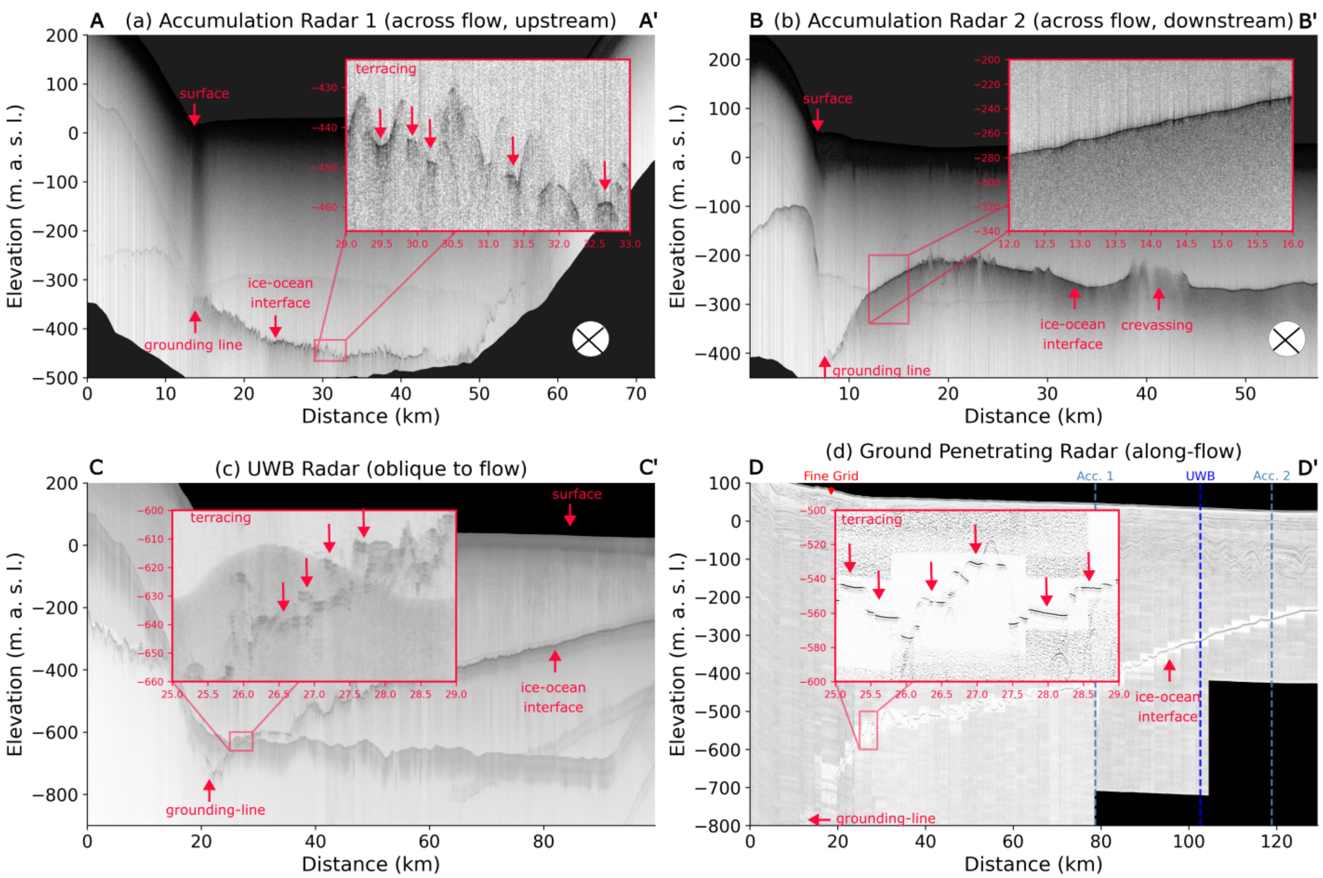


**Figure 2.** Basal terracing and absence thereof across the ice shelf. Airborne (a–c) and GPR profiles (d), with capital letters at the top A–D indicating location shown in Fig. 1. Basal terrace roofs are exemplarily marked with red arrows in insets. They are visible in the accumulation radar in an across-flow transect in the mid-shelf region (a), but no further seaward (b). Ultra-wide band radar detects basal terraces close to the grounding-line and shows a smooth ice–ocean interface further seaward (c). Basal terracing is most evident in the GPR profile, which shows terracing for approximately 90 km into the downstream direction. Further seawards, the ice–ocean interface is smooth, consistent with the airborne data (d).

https://doi.org/10.5194/egusphere-2026-3900
Preprint. Discussion started: 29 July 2026


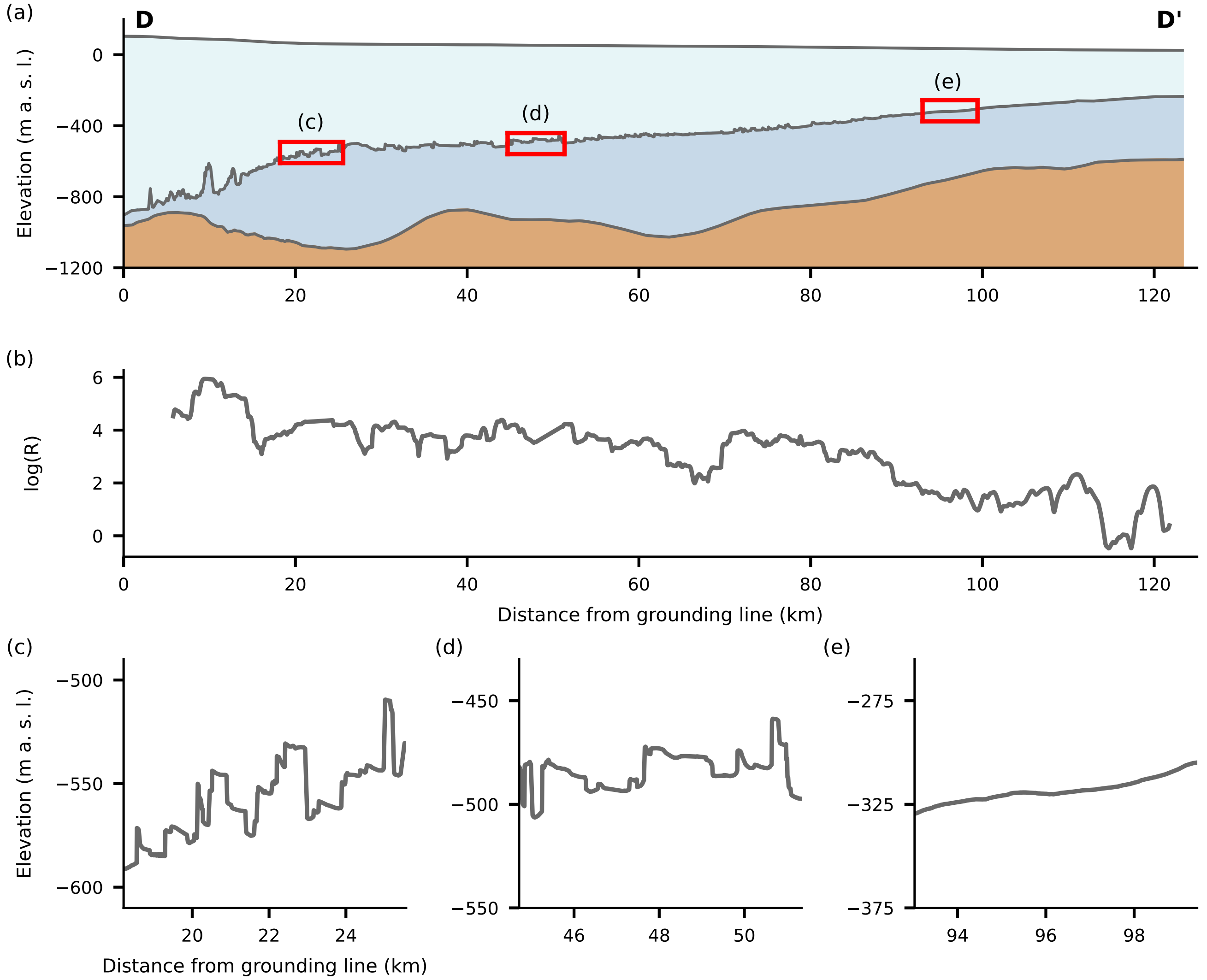


**Figure 3.** Ice-shelf and cavity geometry together with basal roughness. (a) Geometry of ice shelf surface, ice shelf base and bathymetry at the along-flow GPR transect. Both the elevation of the ice-shelf surface and bathymetry are taken from Bedmachine (version 4, Morlighem et al., 2019; Morlighem, 2025). The elevation of the ice-shelf base is derived from the along-flow GPR transect (Fig. 1). (b) Logarithm of basal roughness of the ice shelf base along flow. (c)–(e) Zoom-in on ice–ocean interface shown in (a). The roughness decreases with increasing distance from the grounding line (b, note the logarithmic scale on the y-axis).

https://doi.org/10.5194/egusphere-2026-3900
Preprint. Discussion started: 29 July 2026


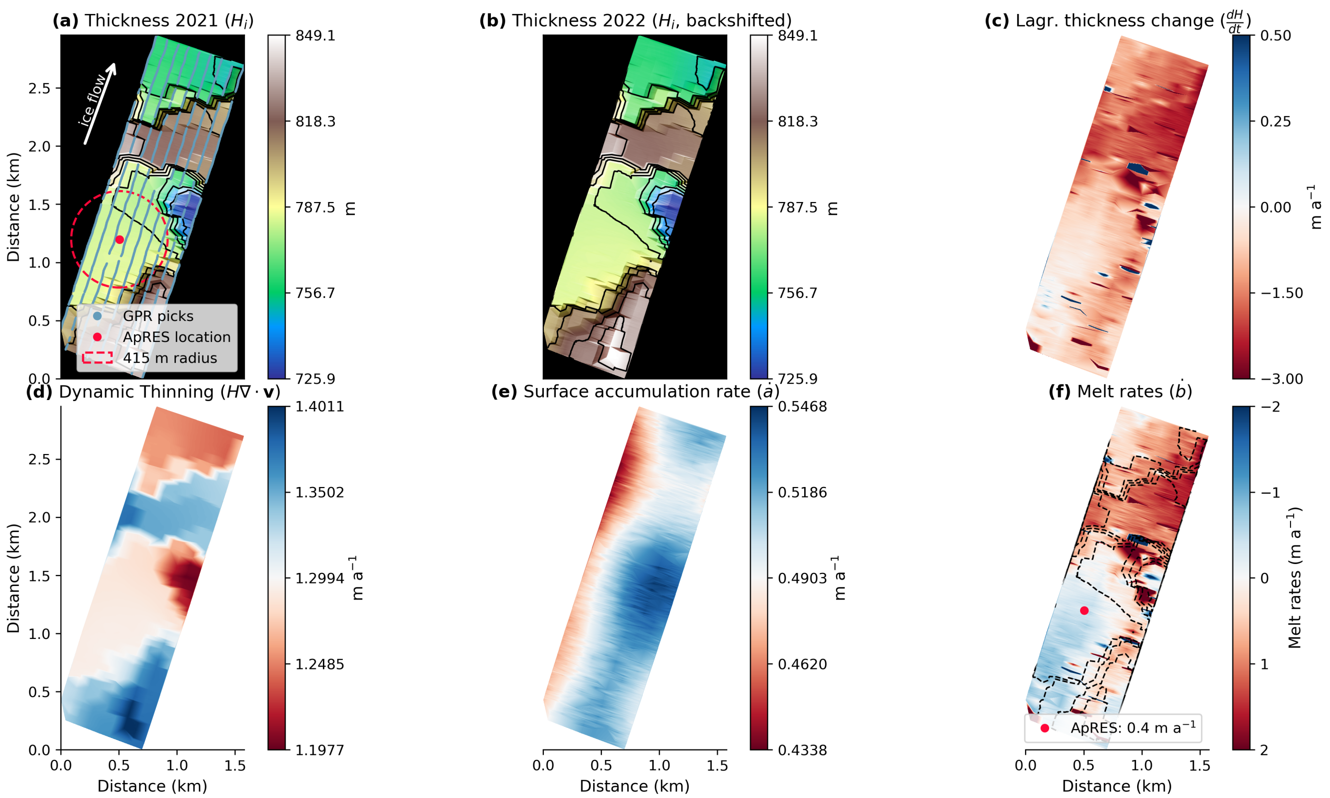


**Figure 4.** Individual terms for the derivation of the Lagrangian basal melt rates. (a) Ice thickness in 2021/22, (b) ice thickness in 2022/23, (c) Lagrangian thickness change between both seasons, (d) flux divergence based on ApRES measurements, (e) surface accumulation rates, and (f) basal melt rates. Absolute uncertainties of these melt rates are larger than $\pm$ 1 m a$^{-1}$ so that the suggested refreezing signal is not significant. The ApRES derived basal melt rates indicate $0.4 \pm 0.03$ m a$^{-1}$ mass loss.

The 3D geometry of terraces becomes evident in the interpolated thickness field derived from the dense grid (Fig. 4a). Terrace walls can be traced coherently between profiles and exhibit a jagged pattern in the horizontal plane. Their overall orientation is oblique to the local ice-flow direction. In contrast, terrace roofs appear as kilometer-scale planar surfaces with minimal horizontal slope. The relief between different features can be up to 120 m. The GPR-derived thickness grid shows that the ApRES instrument positioned at the ice–shelf surface is located centrally over one of these terrace roofs, providing the spatial context for the record of basal melt rates discussed below.

The line spacing of 1.5 km in the coarse grid does not allow for imaging the basal topography in 3D, nevertheless indicates the lateral existence of basal terraces (Fig. 5). Basal topography 1.5 km to either side of the dense grid is jagged again, with abrupt topographic changes, thus basal terraces are visible. However, the topography of neighbouring profiles looks different from each other, and terrace roofs and walls cannot be traced across the 1.5 km profile spacing. The coarse GPR profile furthest to the west (Fig. 5) appears smoother compared to the other lines of the coarse grid. From the dense grid towards the grounding

https://doi.org/10.5194/egusphere-2026-3900
Preprint. Discussion started: 29 July 2026


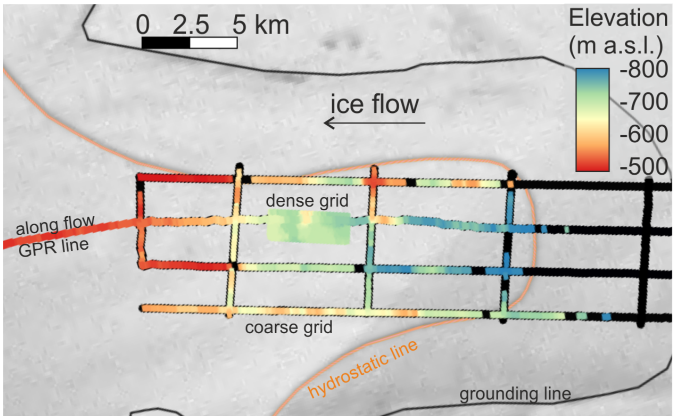


**Figure 5.** Basal topography derived from the coarse and dense GPR grids. Plan view of basal elevation. Black segments along the coarse-grid profiles indicate areas where the bed reflection could not be identified in the radar data, for example, upstream of the hydrostatic line.

line, basal topography gets smoother; however, the ice–shelf base is not coherently visible in the radar data upstream of the grounding line (Fig. A1).

### 4.2 Spatiotemporal basal melt rates at terraces roofs and walls

The most striking observation of the two GPR time slices (Fig. 4a, b) is that the terrace geometry has essentially not changed over the duration of one year. The jagged nature, both in the vertical and the horizontal directions, is evident in both datasets at the profile-to-profile level throughout the grid. Consequently, the Lagrangian thickness change shows no clear signatures of basal terrace formation or evolution, with the exception that the more southerly located plateau has experienced slightly less thinning (Fig. 4c). Approximately half of the overall thickness change is caused by stretching of the ice shelf (Fig. 4d), and the surface accumulation varies less than 10 % across the dense grid. The basal melt rates, calculated as the residual from all of these terms, are on average about 1 m a$^{-1}$. The southern terrace roof suggests minimal refreezing; however, this lies within the method's uncertainty (section 5.2). Regardless of the uncertainty of the method, the relative differences in basal melt between the two terrace roofs are robust and highlight spatial variability in basal melt within the area of the dense grid, despite indicating modest refreezing in other areas.

The reflection at the ice–ocean interface in the ApRES data, acquired above a terrace roof is clear, coherent and single-peaked (Fig. 6b) and we traced it unambiguously over the entire record. The yearly averaged vertical strain rate is $\dot{\varepsilon}_z = -1.65 \cdot 10^{-3}$ a$^{-1}$, indicating vertical thinning of the ice column. The corresponding melt rates are $0.42$ m a$^{-1}$. In comparison, the melt rate from mass conservation, inferred above, is slightly negative ($-0.37$ m a$^{-1}$) at this location, indicating modest basal refreezing. However, both methods agree within the estimated uncertainty bounds. The weekly variability in basal melting ranges between $0.7$ m a$^{-1}$ and $0.1$ m a$^{-1}$ and oscillates most strongly on monthly timescales (Fig. 6d).

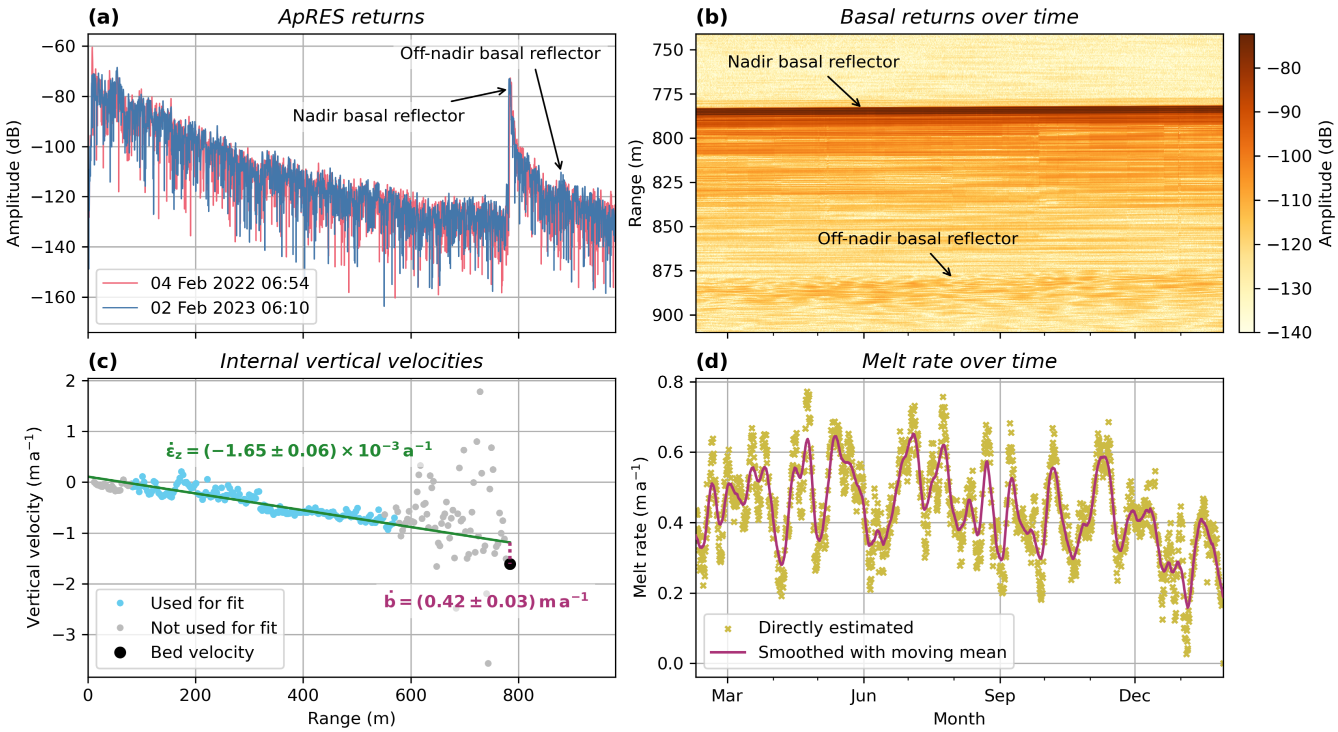


**Figure 6.** ApRES measurements and derived basal melt rates. (a) ApRES return amplitudes from the beginning and the end of the measurement period. (b) Time series of ApRES return amplitude zoomed in on the basal reflection. An increase in amplitude above approximately 880 m in range indicates an off-nadir reflection. (c) Vertical velocities of 6 m bins from cross-correlation of consecutive measurements. The derived velocities are derived using the full ApRES time series and therefore represent an annual average. Grey dots are excluded in the fit, because they are in the uppermost 80 m and mostly within the firn column, or they show a mean correlation less than our applied threshold of 0.95. The slope of the fitted function equals the vertical strain rate, the difference between the linear fit evaluated at the initial bed depth and the real vertical displacement rate of the bed measured at the repeat visit corresponds to the basal melt rate. (d) Time series of basal melt rate. Single data points are derived using one week of ApRES measurements. The dataset is subsequently smoothed with a one-week running mean.

The time series of backscattered power suggests another, less-coherent return at larger traveltimes than the basal return from the terrace roof. As we discuss later in more detail, such a return could originate from an off-nadir reflection similar to what has been observed on other ice shelves (Vaňková et al., 2021; Zeising et al., 2024).

https://doi.org/10.5194/egusphere-2026-3900
Preprint. Discussion started: 29 July 2026


# 5 Discussion

## 5.1 Spatial distribution of basal terraces in warm and cold cavity ice shelves

The combined airborne and GPR data provide a consistent picture: at Ekström Ice Shelf, basal terraces occur at the grounding zone and advect several tens of kilometres downstream until they disappear. Their amplitude gradually diminishes with increasing distance until they vanish entirely. These observations agree with results from Thwaites Ice Shelf (Schmidt et al., 2023) and appear consistent with Roi Baudouin Ice Shelf, although basal terracing there has not yet been systematically examined: At Roi Baudouin Ice Shelf, radar profiles near the grounding zone (e.g., Fig. 1 in Zhou et al. (2025); Fig. 3 in Drews et al. (2017)) and in the mid-shelf region (Fig. 3 in Koch et al. (2023)) display basal terraces as defined here, whereas profiles from the ice–shelf front (Fig. 5 in Drews (2015); Fig. 6 in Drews et al. (2020)) predominantly show a smooth ice–ocean interface. This spatial pattern may therefore be characteristic of many ice shelves that exhibit basal terracing. Notably, Ekström and Roi Baudouin are cold-cavity ice shelves, while Thwaites and Dotson (Wåhlin et al., 2024) are warm-cavity ice shelves. Similarly, observations beneath Dotson are from the ice–shelf edge, suggesting that surface water warming during austral summer affcts their formation. This oceanographic settings contrasts with our observation of basal terraces near the ice-shelf grounding zone and suggests that the initiation of basal terracing is unlikely to depend on far-field ocean forcing and instead reflects a more localized process.

The advection of basal terraces and their gradual decrease is one component that determines the exponential decrease in basal roughness with distance to the grounding line. The known melt rates along the central flow line of Ekström Ice Shelf (Moss et al., 2025), however, stay near-constant within a band of 0–1 m a$^{-1}$. Consequently, we do not see a correlation between basal roughness and basal melt. The gradual downstream decrease in terrace amplitude may result from changing oceanographic conditions, such as variations in thermocline depth that alter the vertical distribution of ocean heat available for basal melting (Kimura et al., 2017), from the progressive modification of neighbouring terraces through continued melting, or from internal ice deformation associated with longitudinal stretching (Fig. C1) and viscous creep as the ice flows toward the unconfined shelf front (Larter, 2022) which can reduce the amplitude of basal topography during downstream advection (Gladish et al., 2012). The data shown here do not allow us to unequivocally distinguish between these mechanisms, and further oceanographic observations together with repeat measurements are needed to identify the dominant processes driving this gradual decrease.

Although our data do not capture the initial formation of basal terraces, they are already present within 1 km downstream of the satellite-inferred grounding line. If basal melting is the driving mechanism, localized melt rates of several tens of meters per year (Shean et al., 2019; Ciracì et al., 2023; Washam et al., 2019) would be required within a relatively narrow region in the grounding zone. Given that the terrace topography appears nearly time-invariant in our high-resolution grid, the governing process likely weakens or ceases with increasing distance from the grounding zone.

## 5.2 Spatio-temporal variability in basal melting of a terrace field

The mass-balance-derived melt rates within the dense grid are subject to both absolute and relative uncertainties. As noted in previous studies (Moholdt et al., 2014; Berger et al., 2017), properly accounting for horizontal advection is a major source

https://doi.org/10.5194/egusphere-2026-3900
Preprint. Discussion started: 29 July 2026


of absolute error, especially where ice thickness variability is large. Systematic thickness offsets between terrace walls, for example, would appear as sharp anomalies in the inferred basal melt-rate field. In our case, matching internal radar reflection horizons yields an ice–shelf velocity of 154 m $a^{-1}$, which is 10 m $a^{-1}$ higher than satellite-derived velocities (146 m $a^{-1}$ Mouginot et al., 2019) and estimates from ApRES device advection (also 146 m $a^{-1}$). Given the 5 m along-track spacing of the GPR data, however, these differences are small and are addressed by interpolating second-season radar points onto those from the first season. Thus, correcting for ice advection through internal-layer matching or through satellite- and ground-based velocity measurements leads to essentially the same result. We are therefore confident that horizontal advection is adequately accounted for in our workflow. Nonetheless, pointwise interpolation alters the mean ice thickness by 0.3 m, surface accumulation rates are not fully constrained, and uncertainties associated with manual picking over the relatively rough basal topography span several radar bins. Together, these factors contribute to a cumulative absolute uncertainty of at least ±1 m $a^{-1}$ for the mass balance approach. Consequently, the difference of 0.6 m $a^{-1}$ between ApRES-derived melt rates and the refreezing signal inferred from the mass balance approach lies within the expected uncertainty range of the latter, and is not considered statistically significant.

While the absolute melt rate values inferred from the mass balance approach exhibit higher uncertainty, the spatial variability and relative differences of these melt rates are more robust. The south–north gradient toward higher downstream melt rates, therefore, represents a meaningful signal and provides spatial context for the localized ApRES measurements. This approach underscores the potential of complementing high-quality point estimates from ApRES with repeat radar profiles to assess the spatial representativeness of ApRES melt rates within a wider study area. Localized melt rates at the terrace roofs are generally low and below the regional average. For comparison, Adusumilli et al. (2020) report 3.2 m $a^{-1}$ for a nearby 500 m × 500 m grid cell, consistent with estimates from internal radar stratigraphy by Moss et al. (2025). These findings align with previously proposed mechanisms such as reduced heat transport to the ice base due to ocean stratification (Davis et al., 2023; Schmidt et al., 2023; Wåhlin et al., 2024).

Compared to melt rate variability in other locations on the Ekström Ice Shelf (Zeising et al., 2025), the amplitude of variations near the grounding zone is weaker, which underlines that seasonality and amplitude of melt rates are dependent on the locations on the ice shelf.

### 5.3 Potential melt signal along terrace walls

Overall, the highest melt rates occur at the deepest terrace roof, while no pronounced signal could be detected at the terrace walls within the limits of the mass balance approach. The potential off-nadir reflection seen in the ApRES time series might originate from a reflection at a neighbouring terrrace wall. In this case, the true depth $d$ must be estimated from the basal geometry inferred from the dense GPR grid. Additionally, it has to be considered that the ice shelf is subject to horizontal strain, which might affect the change in range of an off-nadir reflector. We accounted for this following the analysis of Vaňková et al. (2021) with the assumption that bending is negligible. Furthermore, assuming that melt occurs perpendicular to the reflection

https://doi.org/10.5194/egusphere-2026-3900
Preprint. Discussion started: 29 July 2026


surface, we rewrote the basal melt rate

$$\dot{b} = v_{\text{base}} - (\dot{\varepsilon}_z d + v_{\text{surf}}) \cos\alpha - p\dot{\varepsilon}_x \Delta x \sin\alpha \tag{4}$$

in terms of the range change by the reflector $v_{\text{base}}$, the range change through surface processes $v_{\text{surf}}$, and the off-nadir angle $\alpha$. The parameter $p$ encodes how much the horizontal strain is aligned with the line of sight to the reflector ($p = 0$ is perpendicular, while $p = 1$ is parallel) and $\Delta x$ is the horizontal distance of the reflector to the ApRES. Given the traveltime at which the off-nadir reflector appears and the local ice thickness, it is deduced that the potential reflection stems from a point that is separated approximately 415 m laterally from the nadir reflection (red dashed line in Fig. 4a). Considering the base geometry inferred from the dense GPR grid, the reflecting segment could be an inclined terrace wall with a slope of approximately 30°, which is neighbouring a higher lying terrace roof (dark blue segment in Fig. 4a). With $\alpha$ and $\Delta x$ given by this ray path, a yearly averaged basal melt rate between $3.95\,\text{m a}^{-1}$ and $4.35\,\text{m a}^{-1}$ is calculated, depending on the alignment with the horizontal strain $p$. A seasonal variability cannot reliably be inferred for this reflection.

This potential off-nadir melt rate is approximately one order of magnitude bigger than the nadir melt rate at the terrace roof ($\sim 0.4\,\text{m a}^{-1}$). A meltrate increase with increasing ice–base slope would be consistent with the observations reported by Schmidt et al. (2023) and the simulation results documented by Anselin et al. (2024). However, Schmidt et al. (2023) find at maximum an increase by a factor of three in melt rates when comparing zero-slope faces to faces with a 30° slope. Furthermore, we expect large-scale melting on this range along terrace walls to be visible in the repeat dense radar grid and thus detected using the mass balance approach. Although some uncertainty remains in horizontal positioning and GPR profile matching, the similarity in terrace-wall geometry between time slices suggests negligible geometric change and thus no substantial lateral basal melting. The basal terrace field within our dense grid appears largely dormant, with little evidence of enhanced melting at terrace walls. A higher off-nadir melt rate could originate from a local melt event or outside the dense grid. The amplitude of this off-nadir reflection is weaker and not clear; we therefore can not exclude another origin for this reflection. If intense, localized melting does occur, it is more likely situated farther upstream, closer to the grounding zone.

## 6 Conclusion

Using repeat ground-penetrating radar surveys, continuous ApRES measurements, and airborne radar data, we investigate the topography and temporal evolution of basal terraces beneath Ekström Ice Shelf over annual timescales. Our observations provide the first quasi-three-dimensional repeat mapping of a basal terrace field in a cold-cavity ice shelf and constrain melt rates within a terrace field. Our findings show that terracing occurs in or near the grounding zone, terraces then enter a stagnant mode and gradually diminish until the ice–ocean interface becomes uniformly smooth closer to the ice–shelf front. Taking these observations from a cold-cavity ice shelf together with findings from warm-cavity ice shelves suggests that basal terracing is a widespread process that is not controlled primarily by far-field ocean thermal forcing. Despite the pronounced basal relief, the terrace geometry remained remarkably stable between the two field seasons. Both the repeat GPR surveys and the ApRES observations indicate low (<1 $\text{m a}^{-1}$ and below regional average) basal melt rates at terrace roofs. These observations support

https://doi.org/10.5194/egusphere-2026-3900
Preprint. Discussion started: 29 July 2026


previous hypotheses that stratified ocean conditions suppress vertical heat transport toward near-horizontal ice surfaces. Although a weaker off-nadir reflection in the ApRES data may indicate enhanced melting at a nearby inclined basal wall, its origin could not be conclusively determined. Consequently, our observations do not provide evidence for systematically elevated melt rates along terrace walls. Taken together, our results suggest that basal terraces beneath Ekström Ice Shelf are not necessarily active hotspots of sustained melting. Instead, they likely form in the grounding zone under localized conditions of enhanced basal melting and subsequently enter a comparatively stagnant phase during downstream advection. These findings highlight that the relationship between basal roughness and basal melt is spatially variable and that pronounced basal topography does not necessarily imply ongoing enhanced melting. Future observations closer to grounding zones and over longer time periods as well as surveys with side-looking capabilities to observe wall melting, will be essential to capture the processes responsible for the initiation and early evolution of basal terraces.

https://doi.org/10.5194/egusphere-2026-3900
Preprint. Discussion started: 29 July 2026


*Data availability.* The ApRES time series and derived basal melt rates, and the processed GPR data are available on . Publication on Pangaea for the final revised paper is in progress. The airborne Accumulation radar data (Steinhage et al., 2025) and UWB radar data (Eisen et al., 2024) are accessible through the Marine Data Portal https://marine-data.de/ (Franke et al., 2026). The processed along-flow GPR profiles are available in (Moss et al., 2025).

## Appendix A: Comparison of EMR and GPR data along flow

We use airborne EMR radar data acquired in 2023 and compare it with the along-flow GPR data collected in 2021/22 (Figure A1). Both datasets are spatially referenced using distance from the grounding line as defined by Rignot et al. (2025a):

- The GPR data do not penetrate sufficiently to resolve the ice base between the grounding line and the hydrostatic line. However, they provide high-resolution imaging of the ice base beginning approximately 5 km downstream of the grounding line. In this region, EMR observations reveal basal terraces extending seaward from the grounding line (highlighted in red in panel a).
- Further offshore, the GPR data resolve basal features in greater detail than is possible with the EMR dataset. Between the two survey periods, these basal features appear to have advected approximately 1 km downstream with ice flow (blue panels). Red arrows indicate features identified in both datasets.
- The grounding line delineation from (Rignot et al., 2025a) lies approximately 1 km inland of the position suggested by the strong basal reflection observed in the EMR data. This offset likely reflects a systematic bias in InSAR-derived grounding line products, which tend to map the hinge line upstream of the true grounding line position. The strong basal reflection in the EMR data is instead interpreted as arising from the transition in basal reflectivity as ice becomes afloat over saline ocean water. Consistent with this interpretation, no basal terraces are observed upstream of the grounding line.

## Appendix B: Comparison of repeat GPR data

## Appendix C: Dynamical setting of Ekström Ice Shelf

https://doi.org/10.5194/egusphere-2026-3900
Preprint. Discussion started: 29 July 2026


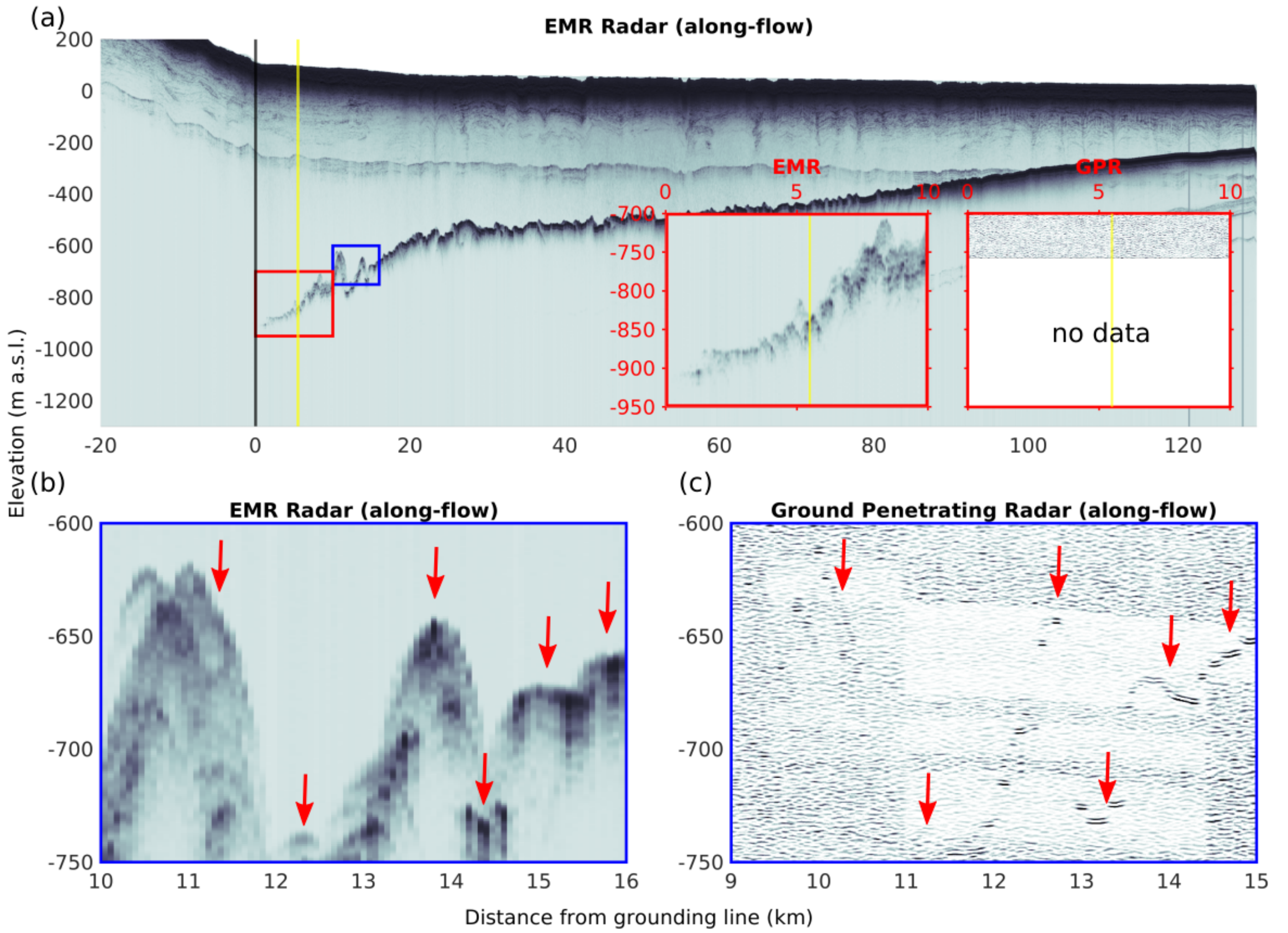


**Figure A1.** Comparison of airborne (EMR) and ground-based (GPR) radargrams along the ice-flow direction. (a) EMR data extend across approximately 20 km of grounded ice and more than 130 km of the floating Ekström Ice Shelf toward the ice front. The red rectangle highlights the tidal flexure zone between the grounding line and the hydrostatic line (after Rignot et al., 2025a), where the GPR data do not image the ice base. In contrast, the EMR data reveal that a rough basal topography is already present close to the grounding line. (b, c) Farther downstream, both the EMR and GPR data image the basal terraces described in the main text. Red arrows highlight characteristic features that can be identified in both datasets. The approximately 1 km spatial offset between the observations is attributed to ice advection between the airborne and ground-based radar surveys.

https://doi.org/10.5194/egusphere-2026-3900
Preprint. Discussion started: 29 July 2026


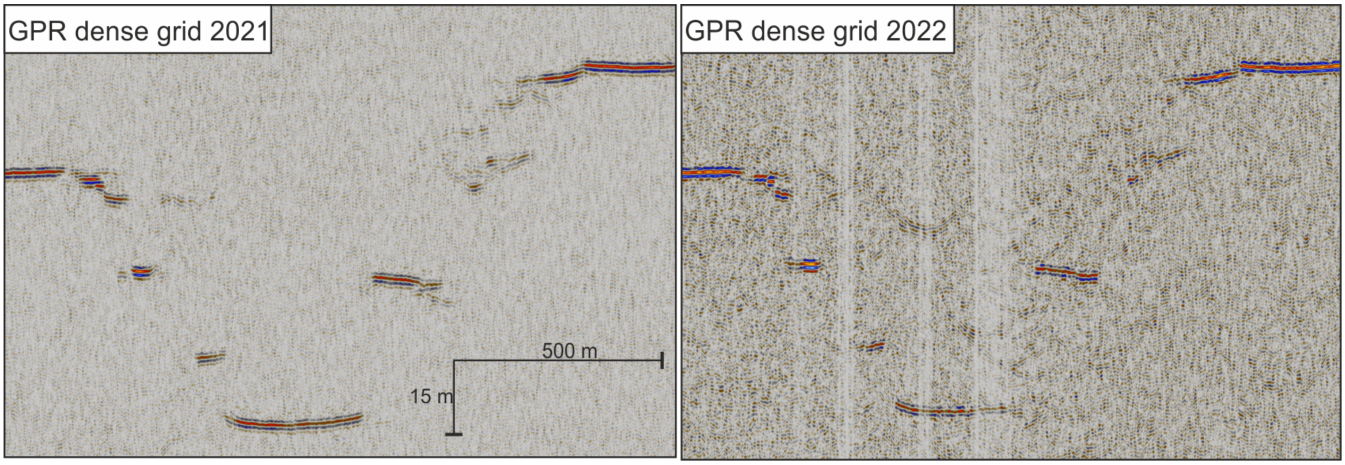


**Figure B1.** Comparison of repeat GPR data showing basal terraces imaged in 2021/22 and 2022/23. The 2022 radar data (right) contains more noise compared to 2021 data. No topographic difference of the basal reflection is visible between the two datasets.

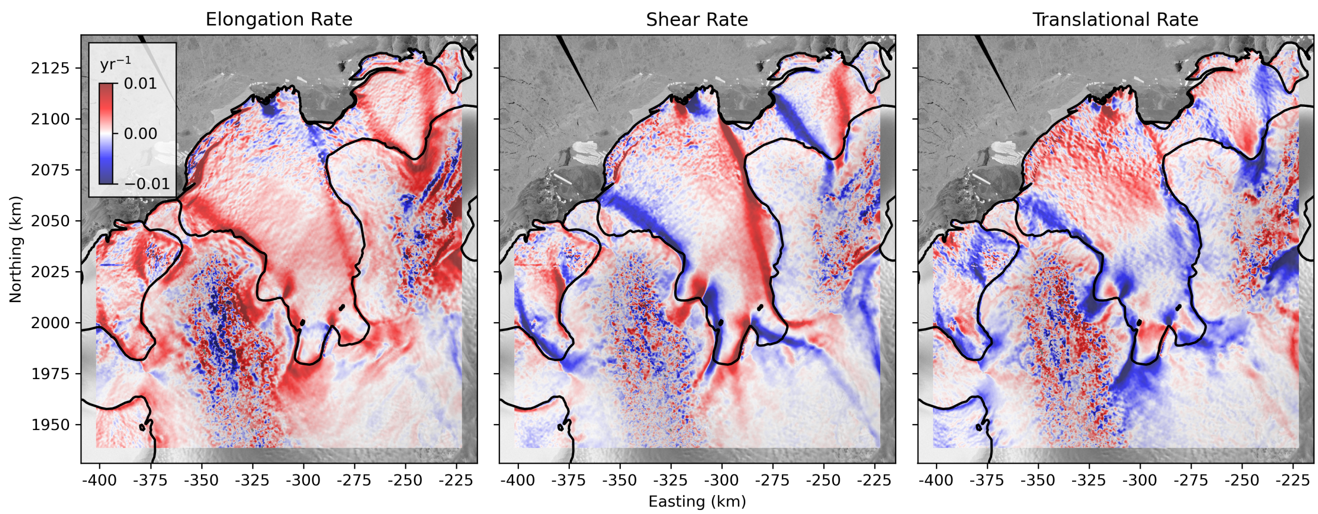


**Figure C1.** Strain rates of Ekström Ice Shelf derived from the MEaSUREs velocity product. (a) Longitudinal strain rates, with red indicating along-flow extension and blue indicating along-flow compression. A localized region of weak longitudinal compression is visible in the western tributary feeding the ice shelf. (b) Shear strain rates, with red indicating dextral shear and blue indicating sinistral shear. (c) Transverse strain rates, where red denotes across-flow extension and blue denotes across-flow compression. The western tributary exhibits pronounced transverse extension, and a transition from across-flow compression to extension is observed approximately 70 km downstream of the grounding line.

https://doi.org/10.5194/egusphere-2026-3900
Preprint. Discussion started: 29 July 2026


*Author contributions.* RS, JN, LSM, CTW, and RD contributed to the conceptualization of the study. FOM, OE, and RD acquired and curated the data. RS, JN, LSM, and RD wrote the original draft. RS, JN, LSM, CTW, OE, and RD reviewed and edited the manuscript. RD administered the project and acquired the funding. All authors read and approved the final manuscript.

*Competing interests.* At least one of the (co-)authors is a member of the editorial board of Natural Hazards and Earth System Sciences.

*Acknowledgements.* Fieldwork was supported by an Emmy Noether grant from the Deutsche Forschungsgemeinschaft (DFG; DR 822/3-1). RS and JN acknowledge financial support from the Baden-Württemberg Stiftung through the Eliteprogramme for Postdocs. We gratefully acknowledge financial support from the Heinrich-Böll-Stiftung for LSM and from the German Academic Scholarship Foundation for FMO. Field observations were further supported by the Alfred Wegener Institute through the logistics grants AWI_ANT_23 (RD) and AWI_ANT_8 (OE). CTW was partially supported by the Deutsche Forschungsgemeinschaft (DFG) in the framework of the priority program 1158 "Antarctic Research with comparative investigations in Arctic ice areas" (grant no. DR 822/8-1). We also acknowledge support from the Open Access Publication Fund of the University of Tübingen. We also acknowledge the use of OpenAI for assistance with manuscript editing. We thank Dr. M. Reza Ershadi, Dr. Inka Koch, and Dr. Jonathan D. Hawkins for their assistance during data acquisition, as well as the staff of Neumayer Station III for logistical support. We are also grateful to the GrouZe team, led by Dr. Tanja Fromm, for their support in the field.

Finally, we gratefully acknowledge Dr. Steven Franke and Dr. Veit Helm for acquiring the UWB radar data and for their valuable contributions to data processing.

https://doi.org/10.5194/egusphere-2026-3900
Preprint. Discussion started: 29 July 2026


## References

Adusumilli, S., Fricker, H. A., Medley, B., Padman, L., and Siegfried, M. R.: Interannual variations in meltwater input to the Southern Ocean from Antarctic ice shelves, Nature Geoscience, 13, 616–620, https://doi.org/10.1038/s41561-020-0616-z, 2020.

Alley, K. E., Scambos, T. A., Siegfried, M. R., and Fricker, H. A.: Impacts of warm water on Antarctic ice shelf stability through basal channel formation, Nature Geoscience, 9, 290–293, https://doi.org/10.1038/ngeo2675, 2016.

Anselin, J., Holland, P. R., Jenkins, A., and Taylor, J. R.: Ice Base Slope Effects on the Turbulent Ice Shelf-Ocean Boundary Current, JOURNAL OF PHYSICAL OCEANOGRAPHY, 54, 1545–1562, https://doi.org/10.1175/JPO-D-23-0256.1, num Pages: 18 Place: Boston Publisher: Amer Meteorological Soc Web of Science ID: WOS:001274738300003, 2024.

Berger, S., Drews, R., Helm, V., Sun, S., and Pattyn, F.: Detecting high spatial variability of ice shelf basal mass balance, Roi Baudouin Ice Shelf, Antarctica, The Cryosphere, 11, 2675–2690, https://doi.org/10.5194/tc-11-2675-2017, 2017.

Brennan, P. V., Lok, L. B., Nicholls, K., and Corr, H.: Phase-sensitive FMCW radar system for high-precision Antarctic ice shelf profile monitoring, IET RADAR SONAR AND NAVIGATION, 8, 776–786, https://doi.org/10.1049/iet-rsn.2013.0053, num Pages: 11 Place: Hertford Publisher: Inst Engineering Technology-Iet Web of Science ID: WOS:000340265100009, 2014.

Ciracì, E., Rignot, E., Scheuchl, B., Tolpekin, V., Wollersheim, M., An, L., Milillo, P., Bueso-Bello, J.-L., Rizzoli, P., and Dini, L.: Melt rates in the kilometer-size grounding zone of Petermann Glacier, Greenland, before and during a retreat, Proceedings of the National Academy of Sciences, 120, e2220924 120, https://doi.org/10.1073/pnas.2220924120, 2023.

Davis, P. E. D., Nicholls, K. W., Holland, D. M., Schmidt, B. E., Washam, P., Riverman, K. L., Arthern, R. J., Vaňková, I., Eayrs, C., Smith, J. A., Anker, P. G. D., Mullen, A. D., Dichek, D., Lawrence, J. D., Meister, M. M., Clyne, E., Basinski-Ferris, A., Rignot, E., Queste, B. Y., Boehme, L., Heywood, K. J., Anandakrishnan, S., and Makinson, K.: Suppressed basal melting in the eastern Thwaites Glacier grounding zone, Nature, 614, 479–485, https://doi.org/10.1038/s41586-022-05586-0, publisher: Nature Publishing Group, 2023.

Davison, B. J., Hogg, A. E., Gourmelen, N., Jakob, L., Wuite, J., Nagler, T., Greene, C. A., Andreasen, J., and Engdahl, M. E.: Annual mass budget of Antarctic ice shelves from 1997 to 2021, Science Advances, 9, eadi0186, https://doi.org/10.1126/sciadv.adi0186, 2023.

Drews, R.: Evolution of ice-shelf channels in Antarctic ice shelves, The Cryosphere, 9, 1169–1181, https://doi.org/10.5194/tc-9-1169-2015, 2015.

Drews, R., Martín, C., Steinhage, D., and Eisen, O.: Characterizing the glaciological conditions at Halvfarryggen ice dome, Dronning Maud Land, Antarctica, Journal of Glaciology, 59, 9–20, https://doi.org/10.3189/2013jog12j134, 2013.

Drews, R., Pattyn, F., Hewitt, I. J., Ng, F. S. L., Berger, S., Matsuoka, K., Helm, V., Bergeot, N., Favier, L., and Neckel, N.: Actively evolving subglacial conduits and eskers initiate ice shelf channels at an Antarctic grounding line, Nature Communications, 8, https://doi.org/10.1038/ncomms15228, 2017.

Drews, R., Schannwell, C., Ehlers, T. A., Gladstone, R., Pattyn, F., and Matsuoka, K.: Atmospheric and Oceanographic Signatures in the Ice Shelf Channel Morphology of Roi Baudouin Ice Shelf, East Antarctica, Inferred From Radar Data, Journal of Geophysical Research: Earth Surface, 125, https://doi.org/10.1029/2020jf005587, 2020.

Dutrieux, P., Vaughan, D. G., Corr, H. F. J., Jenkins, A., Holland, P. R., Joughin, I., and Fleming, A. H.: Pine Island glacier ice shelf melt distributed at kilometre scales, The Cryosphere, 7, 1543–1555, https://doi.org/10.5194/tc-7-1543-2013, 2013.

Dutrieux, P., Stewart, C., Jenkins, A., Nicholls, K. W., Corr, H. F. J., Rignot, E., and Steffen, K.: Basal terraces on melting ice shelves, Geophysical Research Letters, 41, 5506–5513, https://doi.org/10.1002/2014GL060618, _eprint: https://onlinelibrary.wiley.com/doi/pdf/10.1002/2014GL060618, 2014.

https://doi.org/10.5194/egusphere-2026-3900
Preprint. Discussion started: 29 July 2026


Eisen, O., Steinhage, D., Franke, S., Helm, V., Binder, T., Drews, R., Eagles, G., Humbert, A., Jansen, D., Jokat, W., Lambrecht, A., Mieth, M., Riedel, S., and Miller, H.: Collection of datasets from AWI's radio-echo sounding systems on ice sheets and glaciers, https://doi.org/10.1594/PANGAEA.972094, 2024.

Ershadi, M. R., Drews, R., Martín, C., Eisen, O., Ritz, C., Corr, H., Christmann, J., Zeising, O., Humbert, A., and Mulvaney, R.: Polarimetric radar reveals the spatial distribution of ice fabric at domes and divides in East Antarctica, The Cryosphere, 16, 1719–1739, https://doi.org/10.5194/tc-16-1719-2022, publisher: Copernicus GmbH, 2022.

Franke, S., Jansen, D., Binder, T., Paden, J. D., Dörr, N., Gerber, T. A., Miller, H., Dahl-Jensen, D., Helm, V., Steinhage, D., Weikusat, I., Wilhelms, F., and Eisen, O.: Airborne ultra-wideband radar sounding over the shear margins and along flow lines at the onset region of the Northeast Greenland Ice Stream, Earth System Science Data, 14, 763–779, https://doi.org/10.5194/essd-14-763-2022, 2022.

Franke, S., Steinhage, D., Helm, V., Binder, T., Nixdorf, U., Miller, H., Humbert, A., Jansen, D., Eagles, G., Eisermann, H., Jokat, W., Ruppel, A., Drews, R., Zuhr, A., Driemel, A., Walter, A., Konopatzky, P., Heß, R., Haas, A., Koppe, R., Andreas, P. H., and Eisen, O.: Review Article: 30 Years of Airborne Radar Surveys on the Antarctic and Greenland Ice Sheets by the Alfred Wegener Institute, The Cryosphere, 20, 2485–2530, https://doi.org/10.5194/tc-20-2485-2026, 2026.

Fuchs, L. T.: Temporal and Spatial Changes in Snow Accumulation along Kottas Traverse, Dronning Maud Land, East Antarctica,, Ph.D. thesis, Fachbereich Geowissenschaften, Bremen Univeristy, 2026.

Gille, S. T.: Decadal-Scale Temperature Trends in the Southern Hemisphere Ocean, Journal of Climate, 21, 4749–4765, https://doi.org/10.1175/2008JCLI2131.1, 2008.

Gillespie, M. K., Lawson, W., Rack, W., Anderson, B., Blankenship, D. D., Young, D. A., and Holt, J. W.: Geometry and ice dynamics of the Darwin–Hatherton glacial system, Transantarctic Mountains, Journal of Glaciology, 63, 959–972, https://doi.org/10.1017/jog.2017.60, 2017.

Gladish, C. V., Holland, D. M., Holland, P. R., and Price, S. F.: Ice-shelf basal channels in a coupled ice/ocean model, Journal of Glaciology, 58, 1227–1244, https://doi.org/10.3189/2012JoG12J003, 2012.

Greene, C. A., Gardner, A. S., Schlegel, N.-J., and Fraser, A. D.: Antarctic calving loss rivals ice-shelf thinning, Nature, 609, 948–953, https://doi.org/10.1038/s41586-022-05037-w, 2022a.

Greene, C. A., Gardner, A. S., Schlegel, N.-J., and Fraser, A. D.: Antarctic calving loss rivals ice-shelf thinning, Nature, 609, 948–953, https://doi.org/10.1038/s41586-022-05037-w, 2022b.

Grima, C., Koch, I., Greenbaum, J. S., Soderlund, K. M., Blankenship, D. D., Young, D. A., Schroeder, D. M., and Fitzsimons, S.: Surface and basal boundary conditions at the Southern McMurdo and Ross Ice Shelves, Antarctica, Journal of Glaciology, 65, 675–688, https://doi.org/10.1017/jog.2019.44, 2019.

Gudmundsson, G. H., Paolo, F. S., Adusumilli, S., and Fricker, H. A.: Instantaneous Antarctic ice sheet mass loss driven by thinning ice shelves, Geophysical Research Letters, 46, 13 903–13 909, https://doi.org/10.1029/2019GL085027, 2019.

Holland, P. R., Jenkins, A., and Holland, D. M.: The Response of Ice Shelf Basal Melting to Variations in Ocean Temperature, Journal of Climate, 21, 2558–2572, https://doi.org/10.1175/2007JCLI1909.1, 2008.

Jezek, K. C., Farness, K., Carande, R., Wu, X., and Labelle-Hamer, N.: RADARSAT 1 Synthetic Aperture Radar Observations of Antarctica: Modified Antarctic Mapping Mission, 2000, Radio Science, 38, https://doi.org/10.1029/2002RS002643, 2003.

Joughin, I., Shapero, D., Smith, B., Dutrieux, P., and Barham, M.: Ice-shelf retreat drives recent Pine Island Glacier speedup, Science Advances, 7, eabg3080, https://doi.org/10.1126/sciadv.abg3080, 2021.

https://doi.org/10.5194/egusphere-2026-3900
Preprint. Discussion started: 29 July 2026


Kimura, S., Jenkins, A., Regan, H., Holland, P. R., Assmann, K. M., Whitt, D. B., Van Wessem, M., Van De Berg, W. J., Reijmer, C. H., and Dutrieux, P.: Oceanographic Controls on the Variability of Ice-Shelf Basal Melting and Circulation of Glacial Meltwater in the Amundsen Sea Embayment, Antarctica, Journal of Geophysical Research: Oceans, 122, 10 131–10 155, https://doi.org/10.1002/2017JC012926, 2017.

Koch, I., Drews, R., Franke, S., Jansen, D., Oraschewski, F. M., Muhle, L. S., Višnjević, V., Matsuoka, K., Pattyn, F., and Eisen, O.: Radar internal reflection horizons from multisystem data reflect ice dynamic and surface accumulation history along the Princess Ragnhild Coast, Dronning Maud Land, East Antarctica, Journal of Glaciology, 70, https://doi.org/10.1017/jog.2023.93, 2023.

Larter, R. D.: Basal Melting, Roughness and Structural Integrity of Ice Shelves, Geophysical Research Letters, 49, e2021GL097 421, https://doi.org/10.1029/2021GL097421, 2022.

Lindbäck, K., Darelius, E., Moholdt, G., Vaňková, I., Hattermann, T., Lauber, J., and de Steur, L.: Basal Melting and Oceanic Observations Beneath Central Fimbulisen, East Antarctica, Journal of Geophysical Research: Oceans, 130, e2023JC020 506, https://doi.org/10.1029/2023JC020506, _eprint: https://agupubs.onlinelibrary.wiley.com/doi/pdf/10.1029/2023JC020506, 2025.

Malyarenko, A., Wells, A. J., Langhorne, P. J., Robinson, N. J., Williams, M. J., and Nicholls, K. W.: A synthesis of thermodynamic ablation at ice–ocean interfaces from theory, observations and models, Ocean Modelling, 154, 101 692, https://doi.org/10.1016/j.ocemod.2020.101692, 2020.

Mengert, M.: Spatial and temporal variation of snow accumulation along Kottas Traverse, Dronning Maud Land, East Antarctica, Ph.D. thesis, Fachbereich Geowissenschaften, Bremen University, https://doi.org/10.13140/RG.2.2.34493.00481, 2018.

Mitcham, T., Gudmundsson, G. H., and Bamber, J. L.: The instantaneous impact of calving and thinning on the Larsen C Ice Shelf, The Cryosphere, 16, 883–901, https://doi.org/10.5194/tc-16-883-2022, 2022.

Moholdt, G., Padman, L., and Fricker, H. A.: Basal mass budget of Ross and Filchner-Ronne ice shelves, Antarctica, derived from Lagrangian analysis of ICESat altimetry, Journal of Geophysical Research: Earth Surface, 119, 2361–2380, https://doi.org/10.1002/2014jf003171, 2014.

Morlighem, M.: MEaSUREs BedMachine Antarctica, Version 4, 2025.

Morlighem, M., Rignot, E., Binder, T., Blankenship, D., Drews, R., Eagles, G., Eisen, O., Ferraccioli, F., Forsberg, R., Fretwell, P., Goel, V., Greenbaum, J. S., Gudmundsson, H., Guo, J., Helm, V., Hofstede, C., Howat, I., Humbert, A., Jokat, W., Karlsson, N. B., Lee, W. S., Matsuoka, K., Millan, R., Mouginot, J., Paden, J., Pattyn, F., Roberts, J., Rosier, S., Ruppel, A., Seroussi, H., Smith, E. C., Steinhage, D., Sun, B., Broeke, M. R. v. d., Ommen, T. D. v., Wessem, M. v., and Young, D. A.: Deep glacial troughs and stabilizing ridges unveiled beneath the margins of the Antarctic ice sheet, Nature Geoscience, 13, 132–137, https://doi.org/10.1038/s41561-019-0510-8, 2019.

Moss, G., Višnjević, V., Eisen, O., Oraschewski, F. M., Schröder, C., Macke, J. H., and Drews, R.: Simulation-based inference of surface accumulation and basal melt rates of an Antarctic ice shelf from isochronal layers, Journal of Glaciology, 71, e44, https://doi.org/10.1017/jog.2025.13, 2025.

Mouginot, J., Rignot, E., and Scheuchl, B.: MEaSUREs Phase-Based Antarctica Ice Velocity Map, Version 1, https://doi.org/10.5067/PZ3NJ5RXRH10, 2019.

Neckel, N., Drews, R., Rack, W., and Steinhage, D.: Basal melting at the Ekström Ice Shelf, Antarctica, estimated from mass flux divergence, Annals of Glaciology, 53, 294–302, https://doi.org/10.3189/2012AoG60A167, 2012.

Pritchard, H. D., Ligtenberg, S. R. M., Fricker, H. A., Vaughan, D. G., Van Den Broeke, M. R., and Padman, L.: Antarctic ice-sheet loss driven by basal melting of ice shelves, Nature, 484, 502–505, https://doi.org/10.1038/nature10968, 2012.

Reese, R., Gudmundsson, G. H., Levermann, A., and Winkelmann, R.: The far reach of ice-shelf thinning in Antarctica, Nature Climate Change, 8, 53–57, https://doi.org/10.1038/s41558-017-0020-x, 2018.

https://doi.org/10.5194/egusphere-2026-3900
Preprint. Discussion started: 29 July 2026



Rignot, E., Chauche, N., Gadi, R., Ehrenfeucht, S., and Ciraci, E.: Grounding Line Remote Operated Vehicle (GROV) Survey of the Ice Shelf Cavity of Petermann Glacier, Greenland, Geophysical Research Letters, 52, https://doi.org/10.1029/2024gl113400, 2025a.

Rignot, E., Chauche, N., Gadi, R., Ehrenfeucht, S., and Ciraci, E.: Grounding Line Remote Operated Vehicle (GROV) Survey of the Ice Shelf Cavity of Petermann Glacier, Greenland, Geophysical Research Letters, 52, e2024GL113 400, https://doi.org/10.1029/2024GL113400, _eprint: https://onlinelibrary.wiley.com/doi/pdf/10.1029/2024GL113400, 2025b.

Rosevear, M., Galton-Fenzi, B., and Stevens, C.: Evaluation of basal melting parameterisations using in situ ocean and melting observations from the Amery Ice Shelf, East Antarctica, Ocean Science, 18, 1109–1130, https://doi.org/10.5194/os-18-1109-2022, 2022.

Sandmeier Geophysical Software: Reflexw - GPR and seismic processing software, https://www.sandmeier-geo.de/reflexw.html, 2024.

Scambos, T. A., Bohlander, J. A., Shuman, C. A., and Skvarca, P.: Glacier acceleration and thinning after ice shelf collapse in the Larsen B embayment, Antarctica, Geophysical Research Letters, 31, 2004GL020 670, https://doi.org/10.1029/2004GL020670, 2004.

Schannwell, C., Drews, R., Ehlers, T. A., Eisen, O., Mayer, C., and Gillet-Chaulet, F.: Kinematic response of ice-rise divides to changes in ocean and atmosphere forcing, The Cryosphere, 13, 2673–2691, https://doi.org/10.5194/tc-13-2673-2019, 2019.

Schmidt, B. E., Washam, P., Davis, P. E. D., Nicholls, K. W., Holland, D. M., Lawrence, J. D., Riverman, K. L., Smith, J. A., Spears, A., Dichek, D. J. G., Mullen, A. D., Clyne, E., Yeager, B., Anker, P., Meister, M. R., Hurwitz, B. C., Quartini, E. S., Bryson, F. E., Basinski-Ferris, A., Thomas, C., Wake, J., Vaughan, D. G., Anandakrishnan, S., Rignot, E., Paden, J., and Makinson, K.: Heterogeneous melting near the Thwaites Glacier grounding line, Nature, 614, 471–478, https://doi.org/10.1038/s41586-022-05691-0, publisher: Nature Publishing Group, 2023.

Shean, D. E., Joughin, I. R., Dutrieux, P., Smith, B. E., and Berthier, E.: Ice shelf basal melt rates from a high-resolution digital elevation model (DEM) record for Pine Island Glacier, Antarctica, The Cryosphere, 13, 2633–2656, https://doi.org/10.5194/tc-13-2633-2019, 2019.

Smith, E. C., Hattermann, T., Kuhn, G., Gaedicke, C., Berger, S., Drews, R., Ehlers, T. A., Franke, D., Gromig, R., Hofstede, C., Lambrecht, A., Läufer, A., Mayer, C., Tiedemann, R., Wilhelms, F., and Eisen, O.: Detailed Seismic Bathymetry Beneath Ekström Ice Shelf, Antarctica: Implications for Glacial History and Ice-Ocean Interaction, Geophysical Research Letters, 47, e2019GL086 187, https://doi.org/10.1029/2019GL086187, 2020.

Steinhage, D., Humbert, A., Eisen, O., and Braun, M. H.: ANT 2013/14: AWI airborne Accumulation Radar data over wester DML, Sörasen, Recovery Glacier and Antarctic Peninsula (Sör-Mond, RECISL, CoFi Structure, and VELMAP Projects), https://doi.org/10.1594/PANGAEA.983439, 2025.

Stewart, C. L., Christoffersen, P., Nicholls, K. W., Williams, M. J. M., and Dowdeswell, J. A.: Basal melting of Ross Ice Shelf from solar heat absorption in an ice-front polynya, Nature Geoscience, 12, 435–440, https://doi.org/10.1038/s41561-019-0356-0, 2019.

Vaňková, I., Cook, S., Winberry, J. P., Nicholls, K. W., and Galton-Fenzi, B. K.: Deriving Melt Rates at a Complex Ice Shelf Base Using In Situ Radar: Application to Totten Ice Shelf, Geophysical Research Letters, 48, e2021GL092 692, https://doi.org/10.1029/2021GL092692, 2021.

Vaňková, I., Cook, S., Winberry, J. P., Nicholls, K. W., and Galton-Fenzi, B. K.: Deriving Melt Rates at a Complex Ice Shelf Base Using In Situ Radar: Application to Totten Ice Shelf, Geophysical Research Letters, 48, https://doi.org/10.1029/2021gl092692, 2021.

Vaňková, I., Winberry, J. P., Cook, S., Nicholls, K. W., Greene, C. A., and Galton-Fenzi, B. K.: High Spatial Melt Rate Variability Near the Totten Glacier Grounding Zone Explained by New Bathymetry Inversion, Geophysical Research Letters, 50, e2023GL102 960, https://doi.org/10.1029/2023GL102960, _eprint: https://agupubs.onlinelibrary.wiley.com/doi/pdf/10.1029/2023GL102960, 2023.

Višnjević, V., Moss, G., Henry, A. C. J., Wild, C. T., Steinhage, D., and Drews, R.: Mapping the Composition of Antarctic Ice Shelves as a Metric for Their Susceptibility to Future Climate Change, Geophysical Research Letters, 52, https://doi.org/10.1029/2024gl112585, 2025.

https://doi.org/10.5194/egusphere-2026-3900
Preprint. Discussion started: 29 July 2026


Waddington, E. D., Neumann, T. A., Koutnik, M. R., Marshall, H.-P., and Morse, D. L.: Inference of accumulation-rate patterns from deep layers in glaciers and ice sheets, Journal of Glaciology, 53, 694–712, https://doi.org/10.3189/002214307784409351, 2007.

Washam, P., Nicholls, K. W., Münchow, A., and Padman, L.: Summer surface melt thins Petermann Gletscher Ice Shelf by enhancing channelized basal melt, Journal of Glaciology, 65, 662–674, https://doi.org/10.1017/jog.2019.43, 2019.

Watkins, R. H., Bassis, J. N., and Thouless, M. D.: Roughness of Ice Shelves Is Correlated With Basal Melt Rates, Geophysical Research Letters, 48, e2021GL094 743, https://doi.org/10.1029/2021GL094743, 2021.

Wåhlin, A., Alley, K. E., Begeman, C., Hegrenæs, Ø., Yuan, X., Graham, A. G. C., Hogan, K., Davis, P. E. D., Dotto, T. S., Eayrs, C., Hall, R. A., Holland, D. M., Kim, T. W., Larter, R. D., Ling, L., Muto, A., Pettit, E. C., Schmidt, B. E., Snow, T., Stedt, F., Washam, P. M., Wahlgren, S., Wild, C., Wellner, J., Zheng, Y., and Heywood, K. J.: Swirls and scoops: Ice base melt revealed by multibeam imagery of an Antarctic ice shelf, Science Advances, 10, eadn9188, https://doi.org/10.1126/sciadv.adn9188, publisher: American Association for the Advancement of Science, 2024.

Zeising, O., Neckel, N., Dörr, N., Helm, V., Steinhage, D., Timmermann, R., and Humbert, A.: Extreme melting at Greenland's largest floating ice tongue, The Cryosphere, 18, 1333–1357, https://doi.org/10.5194/tc-18-1333-2024, 2024.

Zeising, O., Hattermann, T., Kaleschke, L., Berger, S., Boebel, O., Drews, R., Ershadi, M. R., Fromm, T., Pattyn, F., Steinhage, D., and Eisen, O.: Enhanced basal melting in winter and spring: seasonal ice–ocean interactions at the Ekström Ice Shelf, East Antarctica, The Cryosphere, 19, 2837–2854, https://doi.org/10.5194/tc-19-2837-2025, 2025.

Zhou, Y., Franke, S., Kleiner, T., Drews, R., Humbert, A., Jansen, D., Steinhage, D., and Eisen, O.: Reactivation of a Subglacial Channel Around the Grounding Zone of Roi Baudouin Ice Shelf, Antarctica, Geophysical Research Letters, 52, https://doi.org/10.1029/2024gl112476, 2025.